

## Advanced carrier lifetime analysis method of silicon solar cells for industrial applications



Sang Hee Lee<sup>a</sup>, Kwan Hong Min<sup>a</sup>, Sungjin Choi<sup>a</sup>, Hee-eun Song<sup>a</sup>, Min Gu Kang<sup>a</sup>, Taejun Kim<sup>b</sup>, Sungeun Park<sup>a,\*</sup>

<sup>a</sup> Photovoltaics Laboratory, Korea Institute of Energy Research, Daejeon, 34129, Republic of Korea

<sup>b</sup> Hyundai Energy Solutions, PV R&D Center, Eumseong, Chungju, 27711, Republic of Korea

### ARTICLE INFO

#### Keywords:

Injection-dependent carrier lifetime  
Recombination current density  
PERC solar Cells  
Photoluminescence imaging  
ROI analysis

### ABSTRACT

Over the last few years, the silicon photovoltaic industry has been searching for efficient technologies to reduce the cost of  $\text{cost}/W_{\text{peak}}$  by improving their conversion efficiency. However, with the silicon solar cell efficiency approaching the theoretical limit, it has become important to increase the efficiency distribution of cells by managing the loss factors existing in the production process. Although some companies are managing the efficiency distribution through in-line analysis equipment, a preventive action for reducing process defects has not yet been accomplished. To prevent process defects in advance, big data management is required to correlate the process conditions and solar cell parameters. Hence, an analysis method that can simply evaluate the detailed properties of completed solar cells is a key technique in future PV industries. In this paper, we introduce an advanced injection-dependent carrier lifetime analysis logic that can subdivide detailed recombination factors by fitting the carrier lifetime graph obtained through  $\text{Suns}-V_{\text{oc}}$  measurement with a theoretical graph. The industrial applicability of this analysis method was tested with 160 commercially manufactured solar cells, demonstrating the expected quantitative gains of low-efficiency solar cells. The results show that the proposed method helps in determining the process priority for improving the efficiency distribution and provides a research direction for increasing the absolute efficiency.

### 1. Introduction

In a recent report on photovoltaic (PV) industries, leading products with mono-crystalline silicon wafers exhibited a high efficiency of approximately 22–23% [1]. Although, the efficiency of a silicon solar cell is close to its intrinsic limit (29.1%), there are still active researches for further efficiency improvement to achieve cost competitiveness in the PV market [2,3]. However, the future PV fabrication line will be cost competitive in terms of manufacturing execution systems (MES) by applying in-line analysis equipment. According to this trend, the demand for in-line analysis techniques, such as photoluminescence (PL), electroluminescence (EL), automated optical inspection (AOI), and color inspection, are expected to increase in the PV market.

A simulation result from *Fraunhofer ISE* indicated that increasing the absolute efficiency by 0.05% of the passivated and emitter rear contact (PERC) cell (20.6%) by applying the in-line analysis tool can provide a return on investment of 250 thousand euros within five years [4]. The

investment effect of in-line analysis equipment will not be restricted to efficiency gain. Efficient MES, through in-line analysis equipment, will reduce defective cells in real time and improve efficiency distribution by increasing the number of products that meet the minimum efficiency level. However, except for wafer inspection at the beginning of fabrication, most MES is conducted as a follow-up action. Thus, the fabrication cost of the process is already wasted when defective cells are removed. Therefore, preventive action, which controls various process conditions prior to process defects, should be conducted. To predict process defects, deep learning of big data, which correlates to the process conditions and solar cell parameters, is required. From this perspective, the development of analysis logic, which can extract meaningful information from a fast and simple in-line analysis tool, is necessary for future PV industries.

Therefore, we developed an advanced analysis logic to produce comprehensive information on recombination loss by fitting the real **injection dependent-carrier lifetime (IDCL)** graph with a theoretical

\* Corresponding author.

E-mail address: [separk@kier.re.kr](mailto:separk@kier.re.kr) (S. Park).

IDCL graph. This analysis logic not only can extract the general recombination current densities of the double-diode model ( $J_{01}$ ,  $J_{02}$ ), which is already possible from the Suns- $V_{oc}$  (*Sinton instruments*), but it can also subdivide the detailed components of  $J_{01}$  into the bulk and both side surfaces. In general, evaluation of recombination current density of the doped region near solar cell surfaces requires a measurement of a quasi-steady-state photo-conductance (QSSPC) through the specific sample structure which is symmetrically doped and passivated [5,6]. Therefore, two samples must be prepared separately to obtain recombination current density of both surfaces. However, this method is not suitable to obtain data for industrial level, even though it is a very important technique for the R&D scale. In addition, recombination from the metal-silicon interface cannot be included in this method. For these reasons, we developed a new analysis logic which is suitable for the industrial PV fabrication lines, as it is possible to analyze completed solar cells until metallization.

In Section 2, the theoretical background and procedure of the analysis logic are explained in detail. In addition, a technique that combines PL imaging (PLI) with this analysis logic is introduced to investigate the local defect area on the solar cell. In Section 3, the application results of 160 PERC solar cells, which were commercially fabricated and classified by their efficiency level, are presented. Finally, the causes of degradation of the solar cells in the low-efficiency group are diagnosed.

## 2. Theoretical background and analysis procedure

### 2.1. Analysis principle and logic

The basic analysis principle involves fitting the theoretical effective carrier lifetime ( $\tau_{eff}$ ) graph to the measured  $\tau_{eff}$  graphs. The real IDCL graph can be obtained by measuring Suns- $V_{oc}$ , which produces reliable results for metallized solar cells. Based on the double-diode model, the theoretical  $\tau_{eff}$  can be expressed as the sum of the lifetime in the quasi-neutral region (QNR,  $J_{01}$ ) and space charge region (SCR,  $J_{02}$ ).

$$\frac{1}{\tau_{eff}} = \left( \frac{1}{\tau_{bulk}} + \frac{1}{\tau_{front}} + \frac{1}{\tau_{rear}} \right)_{J_{01}} + \left( \frac{1}{\tau_{SCR}} \right)_{J_{02}} \quad (1)$$

where  $\tau_{bulk}$ ,  $\tau_{front}$ ,  $\tau_{rear}$ , and  $\tau_{SCR}$  are the lifetimes in the bulk, front surface region, rear surface region, and SCR, respectively. For the lifetime of Auger recombination, we applied a generalized model proposed by Kerr et al., even though a model from Richter et al. is more recent version, because Auger recombination lifetime has an ignorable effect on the total effective carrier lifetime [7,8]. Also,  $\tau_{front}$  was substituted as the lifetime in the emitter region ( $\tau_{emitter}$ ) by applying the effective surface recombination velocity ( $S_{eff}$ ), as shown in Equation 6 [9]. In case of the SCR, we applied a model in Equation 10, which describes recombination as a recombination current density [10,11]. For the analysis in this

paper, the ideality factor  $m$  of SCR was fixed as 2, which is physical meaning of  $J_{02}$  and being used by double-diode fitting result of Suns- $V_{oc}$  measurement, because evaluation of the  $m$  value is not applicable in the industrial manufacturing condition. There were gap of evaluated  $J_{02}$  and  $pFF$  values between Suns- $V_{oc}$  results and our IDCL fitting results due to the slight fitting difference (Fig. 1). The  $J_{02}$  values of two analysis had gap of  $1.1 \text{ nA/cm}^2$  on average. Also,  $J_{02}$  gap resulted in  $pFF$  difference of  $0.22 \text{ %p}$ . However, the results are still valid to compare the trend of  $J_{02}$  and  $pFF$  between cell groups.

Also, we applied equation 7 to calculate  $J_{0r}$  by connecting to other fitting parameters ( $J_{01}$ ,  $J_{0e}$ , and SRH lifetime). These parameters can be converted to  $J_{0b}$ , and  $J_{0bl}$ , which are  $J_0$  of effective base region, and  $J_0$  of ideal base region, respectively. The equation 7 was originally derived to define  $J_{0r}$  of aluminum back-surface field (Al-BSF) region by Bowden et al. [12]. The  $J_{0r}$  was derived by applying boundary condition of the Al-BSF edge to the diffusion current density of the base region. For the reason, the analyzed structure is assumed to be full Al-BSF. Therefore, the  $J_{0r}$  results can have difference with those of existing analysis method, because this model determines  $J_{0r}$  by considering only doping density ( $N_B$ ) and bulk lifetime ( $L_B$ ). Although it was not possible to report quantitative difference in this paper, we applied this model to test whether at least a major cause of the recombination surface could be distinguished. The equations for each recombination factor of the  $\tau_{eff}$  are listed in Table 1.

Fig. 2 shows a simplified schematic of  $J_0$  calculation and graph-fitting procedure. To fit the real IDCL graph to the theoretical graph,  $J_{01}$ ,  $J_{0e}$ , SRH lifetime ( $\tau_{SRH}$ ), and  $J_{02}$  were adjusted. In order to adjust  $\tau_{SRH}$ , the  $\tau_{p0}$  value was controlled by assuming that  $\tau_{p0}$  is equal to  $\tau_{n0}$  and the energy level of defect ( $E_d$ ) is equal to the mid bandgap ( $E_i$ ). The real values of substrate resistivity and thickness, which determine bulk lifetime and diffusion length, are applied as basic parameters. The graph fitting logic was designed to change one fitting parameter by applying initial default values of the other fitting parameters. Whenever the fitting parameter is changed, a new  $J_{0r}$  is calculated and converted to the recombination lifetime of the rear surface ( $\tau_{rear}$ ) by using Equation 9. The IDCL graph fitting starts after the theoretical carrier lifetime including the  $\tau_{rear}$  is calculated. The graph fitting algorithm completes when the route-mean-square-error (RMSE) value shows the minimum value.

Then, there will be multiple combinations of  $J_{0e}$  and  $J_{0r}$  within the range of RMSE. In order to prevent multiple combinations of  $J_{0e}$  and  $J_{0r}$  with similar quality of graph fitting, the  $V_{oc}$  matching steps are included. This step will lead to obtain single fitting results when two  $V_{oc}$  values are matched. The  $V_{oc}$  matching steps are being conducted by comparing two  $V_{oc}$  values. One is calculated from the Suns- $V_{oc}$  curve converted from the fitting result of the IDCL graph ( $V_{oc,1}$ ), and the other is extracted from the pseudo I-V curve calculated from the double diode equation using the fitted  $J_{01}$  and  $J_{02}$  values without concerning series resistance ( $V_{oc,2}$ ).

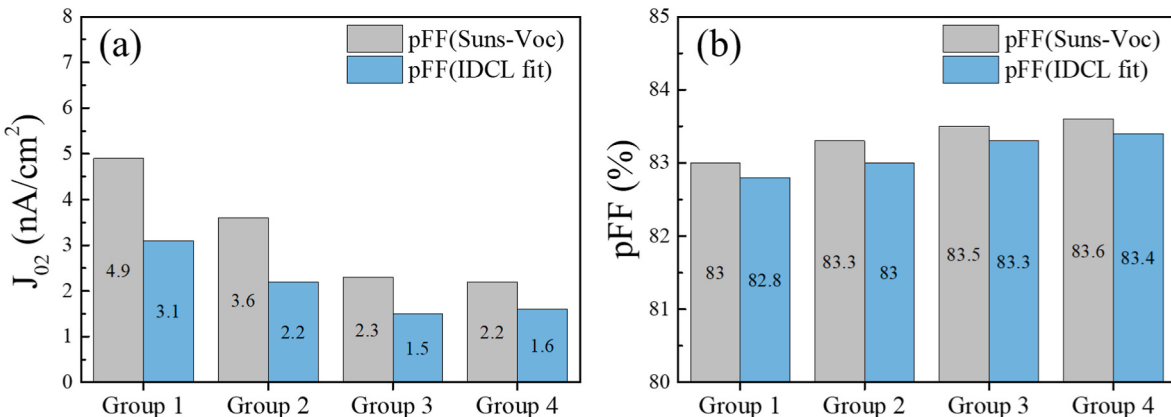


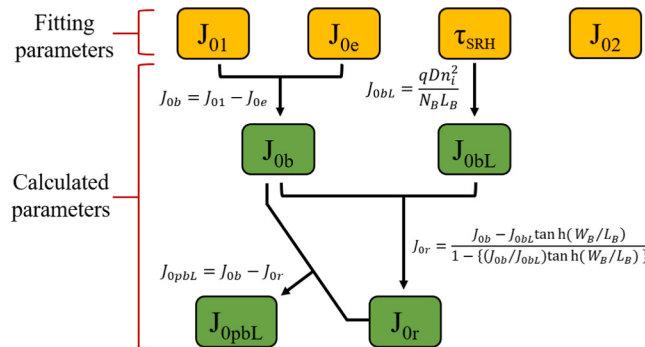
**Fig. 1.** Comparison of (a)  $J_{02}$  and (b)  $pFF$  results between Suns- $V_{oc}$  and IDCL fitting method.

**Table 1**

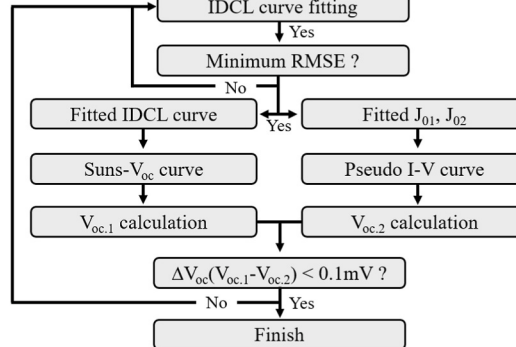
Theoretical equations and definitions of the effective carrier lifetime components.

Components	Equations	No.
Bulk	$\frac{1}{\tau_{bulk}} = \frac{1}{\tau_{rad}} + \frac{1}{\tau_{Auger}} + \frac{1}{\tau_{SRH}}$	(2)
Radiative	$\frac{1}{\tau_{rad}} = B(p_0 + n_0 + \Delta n)$	(3)
Auger	$\frac{1}{\tau_{Auger}} = \frac{(p_0 + \Delta p)(n_0 + \Delta n)(p_0^{0.65} 1.8 \times 10^{-24} + n_0^{0.65} 6 \times 10^{-25} + \Delta n^{0.83} \times 10^{-27})}{\Delta n}$	(4)
Shockley-Read Hall (SRH)	$\frac{1}{\tau_{SRH}} = \frac{p_0 + n_0 + \Delta n}{\tau_{p0}(n_0 + n_1 + \Delta n) + \tau_{n0}(p_0 + p_1 + \Delta p)}$	(5)
(emitter)	$\frac{1}{\tau_{emitter}} = \frac{S_{eff(front)}}{W} = \frac{J_{0e}(N_B + \Delta n)}{qWn_i^2}$	(6)
Rear surface	$J_{0r} = \frac{J_{0b} - J_{0bL} \tanh(W_B/L_B)}{1 - \{(J_{0b}/J_{0bL}) \tanh(W_B/L_B)\}}$	(7)
	$J_{0bL} = \frac{qDn_i^2}{N_B L_B}$	(8)
	$\frac{1}{\tau_{rear}} = \frac{S_{eff(rear)}}{W} = \frac{J_{0r}(N_B + \Delta n)}{qWn_i^2}$	(9)
SCR	$S_{SCR} = \frac{J_{02}}{q\Delta n} [(\Delta n/n_0)^{1/m} - 1]$	(10)
	$\frac{1}{\tau_{SCR}} = \frac{S_{SCR}}{W}$	(11)
Definitions	$\tau_{rad}$ = Radiative recombination lifetime $\tau_{Auger}$ = Auger recombination lifetime $\tau_{SRH}$ = SRH recombination lifetime $B$ = Radiative recombination coefficient $n_i$ = $E_t$ dependent electron concentration $p_i$ = $E_t$ dependent hole concentration $n_0$ = Equilibrium electron concentration $p_0$ = Equilibrium hole concentration $\Delta n$ = Excess electron concentration $\Delta p$ = Excess hole concentration $\tau_{n0}$ = Electron (SRH recombination) lifetime	$\tau_{p0}$ = Hole (SRH recombination) lifetime $J_{0e}$ ( $J_{0f}$ ) = $J_0$ of the emitter (front) surfaces $J_{0r}$ = $J_0$ of the rear surface $J_{0b}$ = $J_0$ of the base region (bulk & rear) $J_{0bL}$ = $J_0$ of the ideal base region $S_{SCR}$ = Recombination velocity in SCR $W$ ( $W_B$ ) = Wafer thickness $L_B$ = Minority carrier diffusion length $N_B$ = Base dopant density $D$ = Minority carrier diffusivity $m$ = Ideality factor of SCR

(a)



(b)

**Fig. 2.** (a)  $J_0$  calculation logic with fitting parameters and (b) fitting procedure of the IDCL graph to determine detailed  $J_0$  of silicon solar cells. (For interpretation of the references to color in this figure legend, the reader is referred to the Web version of this article.)

When the difference of  $V_{oc}$  ( $\Delta V_{oc}$ ) is below 0.1 mV, the total fitting logic is completed. Otherwise, the graph fitting will be conducted again to find the other minimum RMSE value after excluding the previous fitting results. Furthermore, we defined a pseudo  $J_0$  of the bulk region ( $J_{0pbL}$ ), which can be obtained by subtracting  $J_{0r}$  from  $J_{0b}$ , because the total  $J_0$  is composed of  $J_{0e}$  and  $J_{0b}$ . Even though the recombination current density of bulk and rear surfaces cannot be separated through the simple arithmetic,  $V_{oc}$  loss, which is caused by recombination except for two surfaces ( $J_{0e}$ ,  $J_{0r}$ ) in the total  $J_{01}$ , can be expressed by defining the  $J_{0pbL}$ , and this parameter allows an indirect comparison of bulk lifetime between solar cells. Therefore, the  $J_0$  values related to the bulk, emitter (front), rear, and SCR can be evaluated separately by using this logic. In addition, loss analysis of the efficiency and  $V_{oc}$  is possible by applying these  $J_0$  values and short-circuit current density ( $J_{sc}$ ) in the diode equation.

## 2.2. Local area analysis by using PLI

The IDCL graph can also be obtained via the PLI technique along with the Suns- $V_{oc}$  measurement. Fig. 3 depicts the IDCL analysis procedure using the PLI technique. First, the PL images are obtained at the open-circuit condition by varying the illumination intensity (sun) to obtain the IDCL graph. Second, the open-circuit voltage ( $V_{oc}$ ) values at each sun obtained from the Suns- $V_{oc}$  measurement are converted into the excess carrier densities ( $\Delta n$ ) according to Equation (12) [13].

$$\Delta n(N + \Delta n) = n_i^2 \exp\left(\frac{qV_{oc}}{kT}\right) \quad (12)$$

where  $N$  is the dopant density,  $n_i$  is the intrinsic carrier concentration,  $q$  is the elementary charge,  $k$  is Boltzmann's constant, and  $T$  is the absolute temperature. Subsequently, the average values of the PL intensity ( $I$ ) at

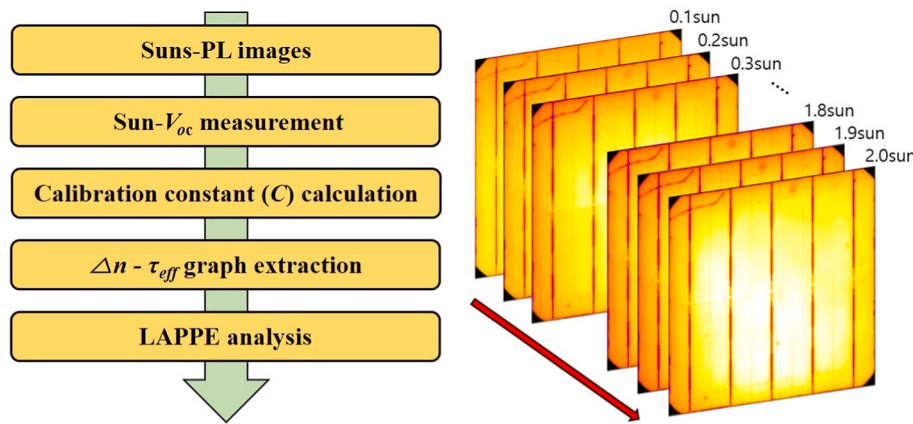


**Fig. 3.** Process of the IDCL analysis by using the PLI (left) and PL images depending on the illumination intensity (right).

each sun are calculated using an arithmetic average method from the PL images. Thereafter, by applying  $\Delta n$  to Equation (13), the calibration constants (C), which correlate the PL intensities with the  $V_{oc}$  values at each sun, are calculated [14].

$$I(\Delta n) = AB\Delta n(N + \Delta n) = C\Delta n(N + \Delta n) \quad (13)$$

where A is a constant factor and B is the coefficient of radiative recombination. Finally, the IDCL graph can be extracted by calculating  $\tau_{eff}$  for all the PL images. The equation for the calculation of  $\tau_{eff}$  is as follows:

$$\tau_{eff} = \frac{n_i^2 \exp(qV_{oc}/kT)}{J_{ph}(N + \Delta n)/qW} \quad (14)$$

where  $J_{ph}$  is the photo-generated current density and W is the sample thickness. The main benefit of this method is that it can analyze the recombination of local areas in the PL image by defining the region of interest (ROI). The  $V_{oc}$  of the ROI for the calculation of  $\tau_{eff}$  can be obtained from the  $V_{oc}$  image, which is converted from the PL image by applying a calibration constant to each pixel. Also,  $J_{ph}$  values of each ROI were obtained by local external quantum efficiency (EQE) measurement within the ROI region, because it was difficult to accurately define the  $J_{ph}$  of the ROI region. Even though there was small variation of effective carrier lifetime depending on the  $J_{ph}$ , it was confirmed that a  $J_{ph}$  variation about 1 mA/cm<sup>2</sup> changes the effective-carrier lifetime of less than 1 μs. This means that the small uncertainty of  $J_{ph}$  of ROI is not significant issue in analyzing the major cause of recombination in the ROI.

### 2.3. Sample preparation and characterization methods

To test the IDCL analysis method, 160 p-type PERC solar cells were used, which were commercially manufactured at the mass production line of *Hyundai Energy Solution Co. Ltd*. All cells were classified into four groups of 40 cells each according to their efficiency levels. The structure of the PERC solar cells and the respective  $J_0$  from various sources are shown in Fig. 4(a). The IDCL graphs of each cell for the analysis (Fig. 4(b)) were obtained by measuring the Suns- $V_{oc}$  (*Sinton Instruments*), which varies the light intensity, by using the decay of a flash lamp. The pseudo efficiency ( $pEff$ ) and fill factor ( $pFF$ ) were calculated by applying the  $J_{sc}$  values of each cell that were measured from the light I-V characteristics. The wafer resistivity and thickness of all PERC cells were 0.8 Ω cm and 170 μm, respectively.

Furthermore, PL images were taken using a laboratory-grade PL imaging tool (*LIS-R3, BT imaging*) for analyzing samples having a large local defect area. The illumination source of the PL imaging tool was a laser with a wavelength of 915 nm. The illumination intensity was varied from 0.03 sun to 2.0 sun by controlling the laser power. Because the EQE curve reflects the recombination amount of the two surfaces and the bulk region, the EQE curves, which were measured in a small or large area (whole cell), were compared to test validity of analysis results.

After the IDCL analysis, the doping profiles of the samples were measured by measuring the electrochemical capacitance-voltage (ECV). To measure the ECV, the metal electrodes on both side surfaces were removed using hydrochloric acid (HCl) and nitric acid (HNO<sub>3</sub>) solutions. The passivation layers were then etched using a diluted hydrofluoric acid (HF) solution.

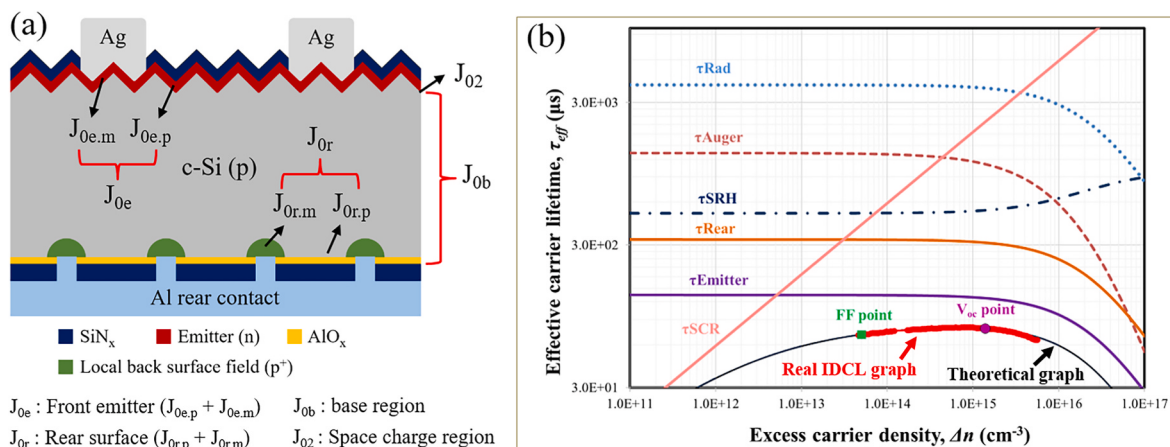


**Fig. 4.** (a) Structure of the p-type PERC solar cell and recombination factors. (b) IDCL graph fitting results.

### 3. Results and discussion

#### 3.1. Advanced IDCL analysis results of 160 p-type PERC solar cells

**Table 2** shows the results of the IDCL analysis of the 160 p-type PERC solar cells. The mean and standard deviation values were summarized for each group. The mean values of  $pEff$  in each group showed a maximum difference of 0.64%, and the decrease in  $V_{oc}$  contributed the most. As shown in the left graph in Fig. 5, a large increase in  $J_{01}$  in group 1 was mainly attributed to the emitter and rear surface recombination. In contrast, the recombination in the bulk showed relatively small and stable values ( $19\text{--}25 \text{ fA/cm}^2$ ) for each group. In addition to the general amount of recombination, the standard deviation increased in the low-efficiency group. In particular, the emitter recombination in group 1 exhibited a significantly larger variation ( $46 \text{ fA/cm}^2$ ) compared to the other groups. Furthermore, three cells with different  $V_{oc}$  levels were randomly selected, and the respective EQE curves were measured by exposing light onto the whole cell area. The image on the right side of Fig. 5 shows the EQE curves and the respective  $J_0$  parameters from the IDCL analysis. The blue and red responses decreased from cell #3 to cell #1, which is consistent with the trends of  $J_{0e}$  and  $J_{0r}$ , respectively.

To investigate the difference in emitter recombination quality in detail, the phosphorous doping profile was measured via ECV after removing the metal electrodes and dielectric layers, as described in Section 2.3. Fig. 6(a) shows the doping profiles of the three PERC solar cells shown in Fig. 5. The ECV was measured at three points in each cell. However, the result of the center point was only included in this study because there was no different trend. The increase in calculated emitter sheet resistance values compared to the initial values may be due to the wet etching of the surface layers. As indicated by the doping profiles, the lower the sheet resistance, the higher the peak dopant concentration and junction depth. The recombination of the heavily doped silicon emitter is mainly determined by the Auger and SRH recombination.

To evaluate the contribution of each factor to  $J_{0e}$ , the EDNA 2 simulation tool, which numerically calculates the recombination in a heavily doped region of silicon, was used [15]. For the simulation, we used commonly used SRH parameters for phosphorous doped emitter as summarized in Table 3 [16,17]. The simulation was conducted by uploading the emitter doping profiles of the three samples and matching the  $J_{0e}$  values between the EDNA and IDCL analysis by varying the surface recombination velocity ( $S_{p0}$ ).  $J_{0e}$  values from the IDCL analysis include both the recombination of passivated emitter ( $J_{0e,p}$ ) and the metal-silicon interface ( $J_{0e,m}$ ). However, the influence of the  $J_{0e,m}$  difference between samples on the trend of simulation results will be relatively small, as the metallized area in commercial solar cells typically occupies about 3% of the front surface. Fig. 6(b) shows that the SRH recombination at the surface dominates the  $J_{0e}$ , while the Auger recombination and SRH recombination at the emitter have relatively very small contributions. In addition, the SRH recombination at the surface increased significantly with low sheet resistance, because the surface recombination velocity was strongly influenced by the dopant concentration of the emitter surface [18].

**Table 2**  
Results of advanced IDCL analysis for each group of 160 p-type PERC solar cells.

Group No.	$pEff$ [%]	$J_{sc}$ [ $\text{mA/cm}^2$ ]	$pFF$ [%]	$V_{oc}$ [mV]	$J_{01}$ [ $\text{fA/cm}^2$ ]	$J_{0e}$ [ $\text{fA/cm}^2$ ]	$J_{0pbL}$ [ $\text{fA/cm}^2$ ]	$J_{0r}$ [ $\text{fA/cm}^2$ ]	$J_{02}$ [ $\text{nA/cm}^2$ ]
1	Mean	21.7	39.80	82.8	656.7	329.2	216.0	18.9	94.2
	Std. Dev.	0.07	0.2	0.46	3.2	41.1	46.0	10.5	19.3
2	Mean	22.0	40.06	83.0	661.5	276.6	175.1	21.6	80.0
	Std. Dev.	0.05	0.11	0.17	1.7	19.0	28.8	8.2	16.9
3	Mean	22.3	40.12	83.2	668.2	217.3	133.9	25.2	58.2
	Std. Dev.	0.04	0.13	0.08	1.0	9.7	17.5	12.0	9.5
4	Ave.	22.5	40.19	83.3	671.8	191.9	122.7	18.9	50.3
	Std. Dev.	0.01	0.05	0.16	0.7	5.7	14.4	2.6	6.4

In addition to quantifying the  $J_0$  of each recombination factor, the contribution of  $V_{oc}$  and  $pFF$  was evaluated as a percentage (Fig. 7). These results are obtained by normalizing the carrier lifetime of each recombination factor with the effective carrier lifetime at two points of  $\Delta n$ , which corresponds to the maximum power point and  $V_{oc}$ . Based on the results, the effect of each recombination factor on the pseudo fill factor and  $V_{oc}$  can be determined.

The contribution of the bulk (Auger, radiative, SRH) recombination on both the  $V_{oc}$  and  $pFF$  points was very small (<10%). In the case of  $V_{oc}$ , the contribution of the emitter recombination accounted for over 60%, which was the largest among the other recombination factors, followed by rear surface recombination (<25%). This trend of contribution on the  $V_{oc}$  point is considered as a general result of the PERC or TOPCon solar cells, which are mainly focused on the reduction of  $J_{0r}$ . Therefore, the reduction of the emitter recombination and improvement of uniformity are required for further improvement of  $V_{oc}$ .

Considering the factors that contributed to the  $pFF$  reduction, the contribution of the SCR increased significantly and almost reached that of the rear surface in the case of the low-efficiency group. This result can also be understood from Fig. 4(b), which shows that the reduction of the carrier lifetime in low-level injection is strongly dependent on the junction leakage current ( $J_{02}$ ) and decrease  $pFF$  [19]. This means that the reduction of junction recombination is also an important target in terms of  $pFF$  improvement. According to the analysis results, it was confirmed that the cells in the low-efficiency group were required to have a lower surface doping concentration in terms of  $J_{0e}$  reduction. In particular, improving the uniformity between the doping processes (or between samples) is a key development point, considering that the deviation of  $J_{0e}$  decreases with higher efficiency groups.

#### 3.2. Analysis results of local areas

IDCL analysis through PLI is beneficial for evaluating the recombination properties of local areas. For the analysis of the local area, two PERC cells, which showed an unusual defect region in the PL image, were selected. Fig. 8 shows the ROIs in the PL images of the two PERC cells and their calculated  $V_{oc}$  (Cal.  $V_{oc}$ ). The Cal.  $V_{oc}$  was evaluated by averaging the  $\Delta n$  of the total pixels in the ROI, because the unit of  $\Delta n$  is changed from  $#/cm^3$  to  $#/pixel$ .

With the first PERC cell, ROI-1 was compared as a reference to ROI-2, which was defined to include the defective area. The IDCL analysis results of ROI-1 and ROI-2 showed that ROI-2 had a higher recombination on the rear surface. The EQE curves in Fig. 8(b), which were measured within the ROI (black lines), show a large EQE drop at long wavelengths. According to this result, it was confirmed that the low PL intensity area in ROI-2 is attributed to the rear surface recombination, and therefore, the IDCL analysis of the local area is possible.

In the case of the second PERC cell, the overall PL intensity was divided into two areas according to the pattern of the front metal grid. Hence, ROI-3 and ROI-4 were defined in the upper and lower half regions of the cell, respectively. The IDCL analysis result of ROI-4 showed higher  $J_{0e}$  ( $30 \text{ fA/cm}^2$ ) and  $J_{0r}$  ( $17 \text{ fA/cm}^2$ ) than that of ROI-3. Although

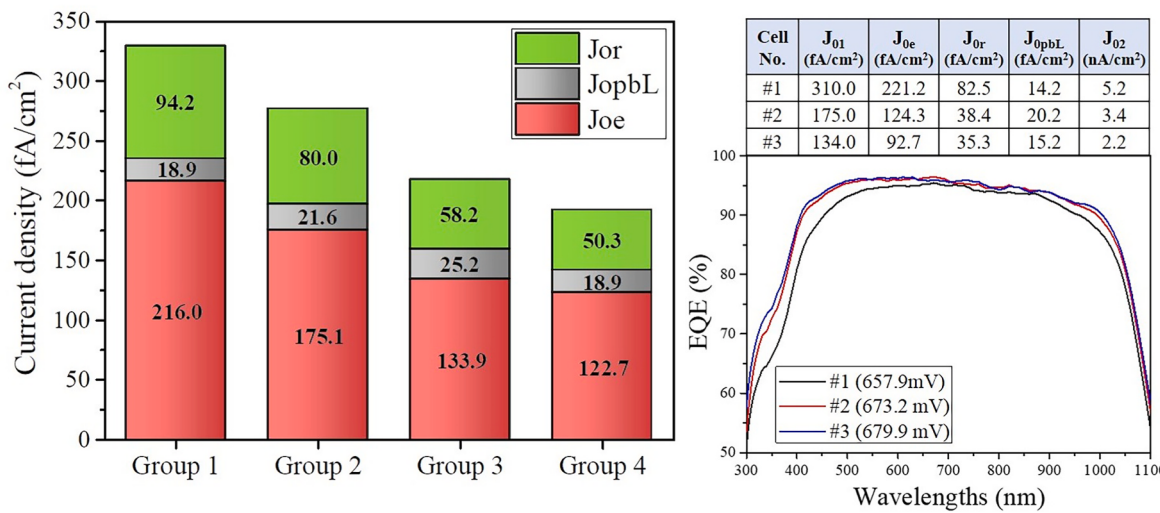


**Fig. 5.** Stacked column graph of the  $J_{0I}$  components (left). Comparison of IDCL analysis and EQE results (right).

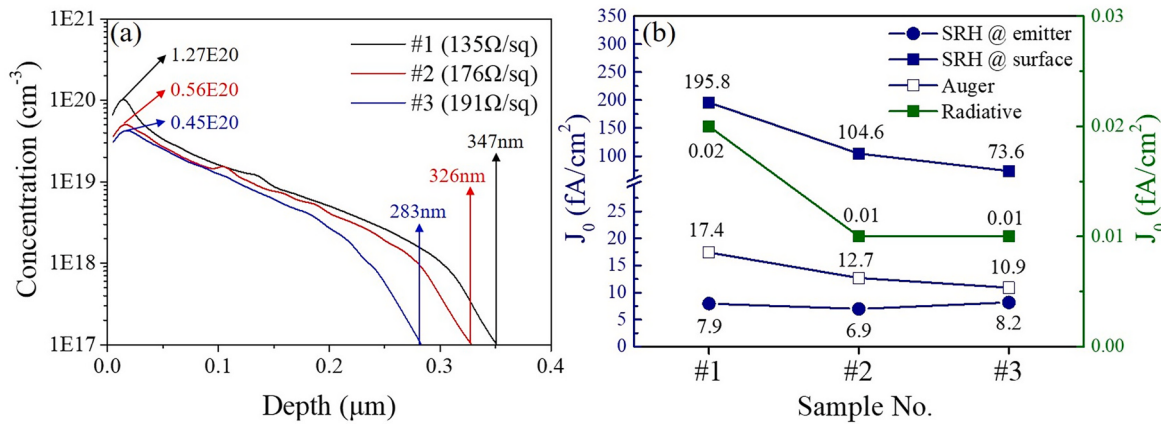


**Fig. 6.** (a) Phosphorous doping profiles and (b) EDNA 2 simulation results of three cells with different emitter recombination.

**Table 3**  
EDNA 2 simulation parameters for separating sources of  $J_{oe}$ .

Cell No.	Emitter SRH				Surface SRH			Outputs	
	$N_{max}$ ( $cm^{-3}$ )	$E_t$	$\tau_{no}$ ( $\mu s$ )	$\tau_{po}$ ( $\mu s$ )	$Q_f/q$ ( $cm^{-2}$ )	$E_t$	$S_{po}$ ( $cm/s$ )	$R_{sh}$ ( $\Omega/sq$ )	$J_{oe}$ ( $fA/cm^2$ )
#1	$1.27 \times 10^{20}$	$E_t = E_i$	100	0.12	$2.8 \times 10^{12}$	$E_t = E_i$	$1.45 \times 10^5$	121	221.2
#2	$0.56 \times 10^{20}$	$E_t = E_i$	100	0.12	$2.8 \times 10^{12}$	$E_t = E_i$	$0.57 \times 10^5$	161	124.3
#3	$0.45 \times 10^{20}$	$E_t = E_i$	100	0.12	$2.8 \times 10^{12}$	$E_t = E_i$	$0.38 \times 10^5$	186	92.7

the difference in rear surface recombination did not appear in the locally measured EQE curve, the front surface recombination within ROI-4 was slightly higher than that in ROI-3. The prominent PL intensity boundary of these two ROIs seems to be attributed to the uniformity of the front metal screen printing or the firing condition, because the metal grids of the upper and lower halves are not connected to each other.

#### 4. Conclusions

In this paper, we proposed an advanced IDCL analysis logic that subdivides the recombination current density of QNR ( $J_{0I}$ ) into the emitter, bulk, and rear surface recombination current densities. In addition, a method that can analyze the local area of the solar cells by combining the IDCL analysis logic with the PLI technique was introduced. This IDCL analysis logic was applied to 160 PERC solar cells, which were commercially manufactured at a mass production line, to

test their effectiveness.

As a result, it was confirmed that the trend of the front and rear surface recombination in the EQE curve reflected the IDCL analysis results well. In the case of samples with large  $J_{oe}$  values, the influencing factor was the increase in the SRH recombination at the surface due to the high phosphorous doping concentration. For the samples with high  $J_{or}$  values, it is possible that rear surface contamination occurred during the wet process, considering the defect geometry in the PL image and EQE results. Based on the analysis results, the quantitative gains, which can be obtained by improving the properties of the solar cells in group 1 to the level of group 4, are summarized below.

- Average  $V_{oc}$  gain of 10.2 mV through the improved dopant diffusion uniformity of each wafer within the process.
- Average  $V_{oc}$  gain of 5.3 mV through the reduction of recombination on the rear surface.

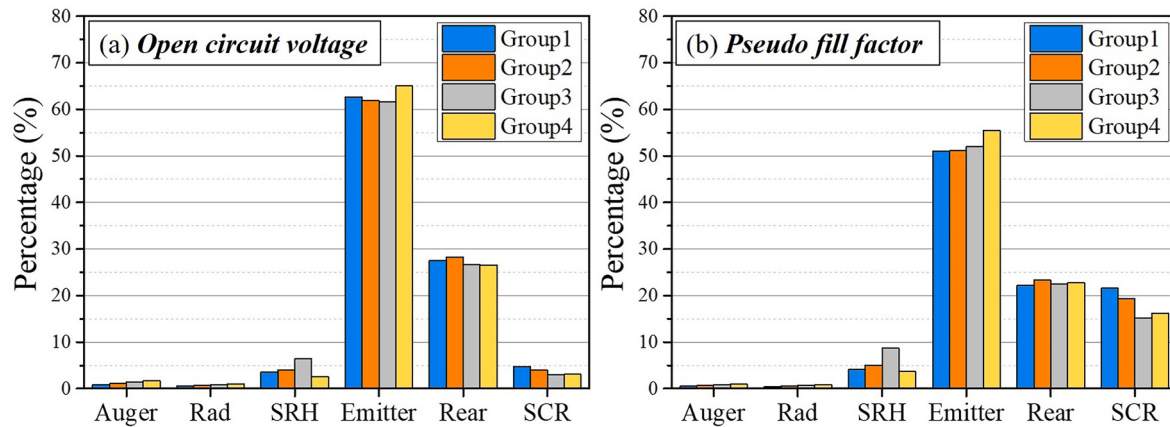


Fig. 7. Contribution rate of each recombination factor to (a) the open circuit voltage and (b) the pseudo fill factor.

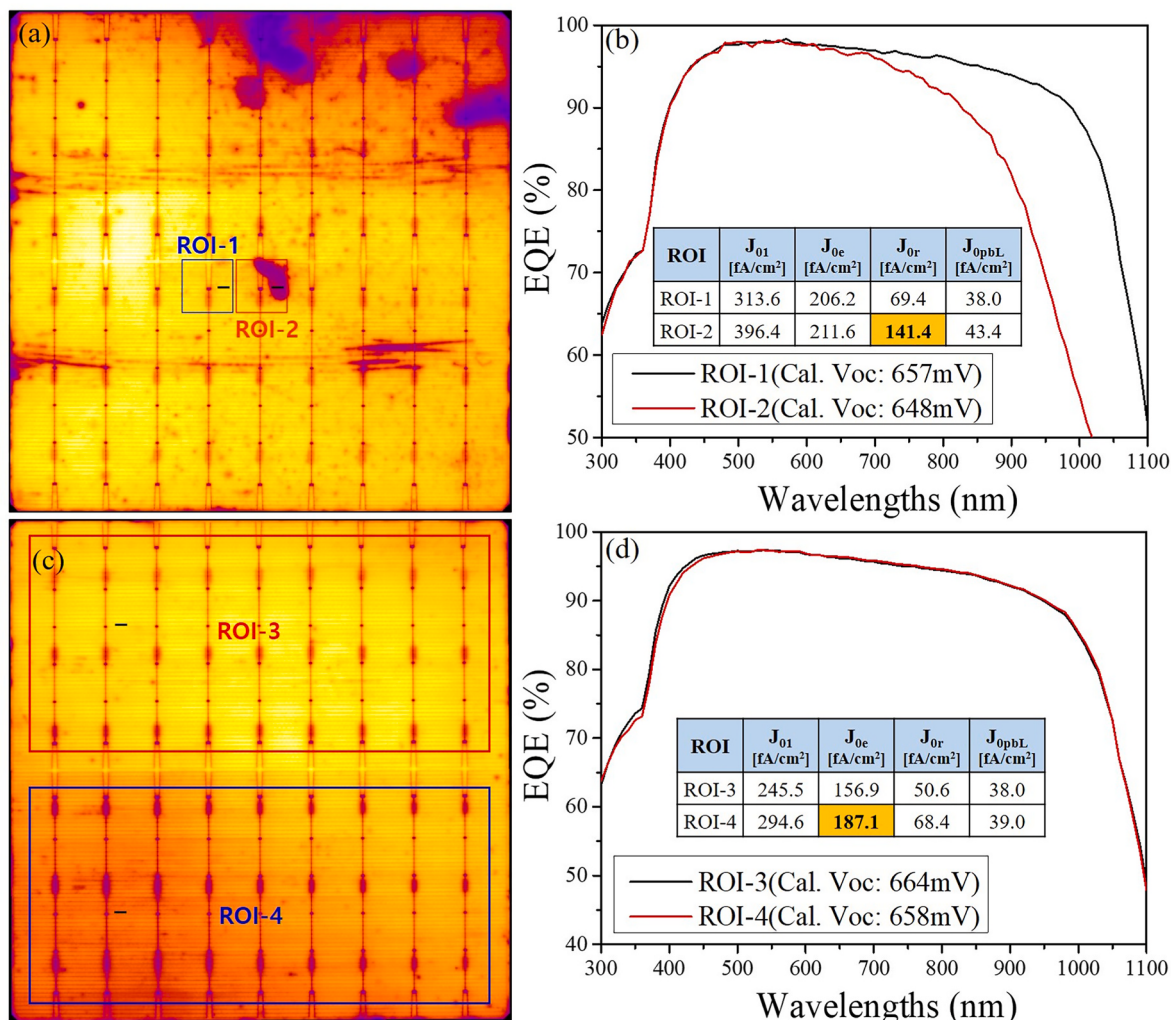


Fig. 8. Results of local IDCL analysis through the PLI; (a, c) location of ROIs and local EQE measurement points (black lines) on the PL images; (b, d) Local EQE curve and the IDCL analysis results (inset table) of the ROIs.

- Average  $pFF$  gain of 0.5 %p through the reduction of junction leakage current accompanied by the emitter/rear surface recombination.
- Average  $pEff$  gain of 0.7 %p through the improved uniformity of emitter/rear surface recombination and optimization of the metal contact.

Although the results of the new IDCL analysis method could not be compared to the results of individual recombination evaluation methods (i.e. symmetrically passivated structure, and  $J_{0m}$  evaluation method), we showed the potential of this analysis method by relatively evaluating the separated  $J_0$  of completed solar cells with EQE results. If this IDCL analysis method is fully verified, the quantitative evaluation of gain in

terms of each recombination factor in a completed cell helps in determining the process priority for improving the efficiency distribution as well as setting the R&D direction towards increasing the absolute efficiency. Furthermore, by using machine learning techniques, big data analysis can be performed by correlating the solar cell parameters with the process conditions and variables (temperature, pressure, gas flow, etc.). We believe that the advanced IDCL analysis logic will play an important role in realizing a smart PV factory in the future.

#### CRediT authorship contribution statement

**Sang Hee Lee:** Writing – original draft, Investigation, Conceptualization. **Kwan Hong Min:** Software, Resources, Methodology. **Sungjin Choi:** Resources. **Hee-eun Song:** Resources, Data curation. **Min Gu Kang:** Resources, Data curation. **Taejun Kim:** Resources. **Sungeun Park:** Supervision, Project administration, Methodology, Conceptualization.

#### Declaration of competing interest

The authors declare that they have no known competing financial interests or personal relationships that could have appeared to influence the work reported in this paper.

#### Data availability

Data will be made available on request.

#### Acknowledgments

This work was supported by the Korea Institute of Energy Technology Evaluation and Planning (KETEP) and the Ministry of Trade, Industry & Energy (MOTIE) of the Republic of Korea (No. 20213030010390).

#### References

- [1] The international Technology roadmap for photovoltaic (ITRPV). <https://itrv.vdma.org>, 2021. (Accessed 10 October 2021).
- [2] M.J. Kerr, A. Cuevas, P. Campbell, Limiting efficiency of crystalline silicon solar cells due to Coulomb-enhanced Auger recombination, *Prog. Photovoltaics Res. Appl.* 11 (2003) 97–104, <https://doi.org/10.1002/pip.464>.
- [3] A. Richter, M. Hermle, S.W. Glunz, Reassessment of the limiting efficiency for crystalline silicon solar cells, *IEEE J. Photovoltaics* 3 (2013) 1184–1191, <https://doi.org/10.1109/JPHOTOV.2013.2270351>.
- [4] J. Haunchild, J. Greulich, H. Hoffler, S. Wasmer, G. Emanuel, A. Krieg, et al., Review of tools and approaches for inline quality control in high efficiency silicon solar cell production, *Proc. 33rd Eur. Photovolt. Sol. Energy Conf. Exhib.* (2017) 870–874.
- [5] D. Kane, R. Swanson, Measurement of the emitter saturation current by a contactless photoconductivity decay method, *Proc. 18th IEEE Photovolt. Spec. Conf.* (1985) 578–583.
- [6] R.A. Sinton, A. Cuevas, M. Stuckings, Quasi-steady-state photoconductance, a new method for solar cell material and device characterization, *Proc. 25th IEEE Photovolt. Spec. Conf.* (1996) 457–460.
- [7] M.J. Kerr, A. Cuevas, General parameterization of Auger recombination in crystalline silicon, *J. Appl. Phys.* 91 (2002) 2473–2480, <https://doi.org/10.1063/1.1242476>.
- [8] A. Richter, S.W. Glunz, F. Werner, J. Schmidt, A. Cuevas, Improved quantitative description of Auger recombination in crystalline silicon, *Phys. Rev. B* 86 (2012), 165202, <https://doi.org/10.1103/PhysRevB.86.165202>.
- [9] C. Reichel, F. Granek, J. Benick, O. Schultz-Wittmann, S. Glunz, Comparison of emitter saturation current densities determined by quasi-steady-state photoconductance measurements of effective carrier lifetimes at high and low injections, *Proc. 23rd Eur. Photovolt. Sol. Energy Conf.* (2008) 1664–1669.
- [10] S.W. Glunz, D. Biro, S. Rein, W. Warta, Field-effect passivation of the SiO<sub>2</sub> Si interface, *J. Appl. Phys.* 86 (1999) 683–691, <https://doi.org/10.1063/1.370784>.
- [11] S. Dauwe, J. Schmidt, A. Metz, R. Hezel, Fixed charge density in silicon nitride films on crystalline silicon surfaces under illumination, *Proc. 19th IEEE Photovolt. Spec. Conf.* (2002) 162–165.
- [12] S. Bowden, D.S. Kim, C. Honsberg, A. Rohatgi, Rapid thermal processing for front and rear contact passivation, *Proc. 29th IEEE Photovolt. Spec. Conf.* (2002) 410–413.
- [13] R.A. Sinton, A. Cuevas, A quasi-steady-state open-circuit voltagage method for solar cell characterization, *Proc. 16th Eur. Photovolt. Sol. Energy Conf.* (2000) 1–4.
- [14] D. Kilani, Luminescence Imaging Techniques for Silicon Photovoltaics, Ph.D. Thesis, 2013.
- [15] K.R. McIntosh, P.P. Altermatt, A freeware 1D emitter model for silicon solar cells, *Proc. 35th IEEE Photovolt. Spec. Conf.* (2010), 002188–002193.
- [16] H. Li, K. Kim, B. Hallam, B. Hoex, S. Wenham, M. Abbott, POCl<sub>3</sub> diffusion for industrial Si solar cell emitter formation, *Front. Energy* 11 (2017) 42–51, <https://doi.org/10.1007/s11708-016-0433-7>.
- [17] A. Nawaz, S. Tahir, A. Alia, M. Arshad, K. Mahmood, S. Siraj, et al., Effect of phosphorus/boron doping profile differences on the performance of silicon solar cells, *J. Ovonic Res.* 16 (2020) 63–70.
- [18] P.P. Altermatt, J.O. Schumacher, A. Cuevas, M.J. Kerr, S.W. Glunz, R.R. King, G. Heiser, A. Schemk, Numerical modeling of highly doped Si: P emitters based on Fermi–Dirac statistics and self-consistent material parameters, *J. Appl. Phys.* 92 (2002) 3187–3197, <https://doi.org/10.1063/1.1501743>.
- [19] J.H. Lee, K.H. Min, M.G. Kang, K.T. Jeong, J.I. Lee, H. Song, S. Park, J. Park, Efficiency characteristics of a silicon oxide passivation layer on p-type crystalline silicon solar cell at low illumination, *Curr. Appl. Phys.* 19 (2019) 683–689, <https://doi.org/10.1016/j.cap.2019.03.006>.